Hydrol. Earth Syst. Sci. Discuss., 8, 1193–1223, 2011
www.hydrol-earth-syst-sci-discuss.net/8/1193/2011/
doi:10.5194/hessd-8-1193-2011

Hydrology and Earth System Sciences Discussions

Inside the hydro-physics processes at the plunge point location: an analysis by satellite and in situ data

A. T. Assireu[1,2], E. Alcântara[1], E. M. L. M. Novo[1], F. Roland[3], F. S. Pacheco[3], J. L. Stech[1], and J. A. Lorenzzetti[1]

[1]Remote Sensing Division, National Institute for Space Research – INPE, CEP12227-010 – Sao Jose dos Campos, SP, Brazil
[2]Natural Resources Institute. Federal University of Itajubá, UNIFEI. Itajubá, Brazil
[3]Aquatic Ecology Laboratory, Biological Science Institute, Federal University of Juiz de Fora, MG, Brazil

Received: 14 December 2010 – Accepted: 16 January 2011 – Published: 26 January 2011

Correspondence to: A. T. Assireu (assireu@gmail.com)

Published by Copernicus Publications on behalf of the European Geosciences Union.

Abstract

The plunge point locates the main point of mixing between river and the epilimnion reservoir water. The plunge point monitoring is essential to understand how it will be the behavior of density currents and its implications for reservoir. The applicability of satellite imagery products from different sensors (Landsat TM band 6 thermal signatures and visible channel) for characterization of the river-reservoir transition zone is presented in this study. We demonstrate the feasibility of the Landsat TM band imagery to discern the subsurface river plumes and the plunge point. The spatial variability of the plunge point evident in the hydrologic data illustrates the advantages of synoptic satellite measurements over in situ point measurements alone to detect the river-reservoir transition zone. It is indicated that the river flowing as underflow contributes to the thermal stability of the water column during wet season (summer-autumn). During the dry season, when the river-reservoir water temperature differences vanish and the river circulation is characterized by interflow-overflow, the river water inserts into the reservoir upper layers, affecting water quality. The results indicate good agreement between hydrologic and satellite data and that the jointly use of thermal and visible channel, operational monitoring of plunge point is feasible. The deduced information about the density current from this product could potentially be assimilated for numerical modeling and hence be of significant interest for environmental and climatological research.

1 Introduction

According to the report published by International Committee of Large Dams (ICOLD – http://www.icold-cigb.net) in 2000, over 40 000 large dams exist in the world with a total storage capacity of 7000 billion m^3. On the other hand, an average rate of 0.5 to 1% of their capacity is lost each year due to sedimentations. Changes due dams can include increased depth, changes in temperature, possible development of density stratification, retention of nitrate and phosphate, growth of plankton and

HESSD
8, 1193–1223, 2011

algae, contaminant trends in sediment, changes in aquatic ecosystem of lotic to lentic, and releasing carbon-based greenhouse gases (Baxter, 1997; Poff and Hart, 2002; Ramos et al., 2006).

Because density of the river water reaching a reservoir usually differs from the density of the water at the reservoir surface, inflows enter and move through reservoir as density currents (Ford, 1990). Temperature, total dissolved solids, and suspended solids can cause density differences. Depending on the density difference between the inflows and ambient waters, the density currents in a reservoir can flow into the downstream area with overflow, underflow, and interflow types (Martin and McCutheon, 1999).

Thus, after the inflow plunges the river, it can follow the thalweg as an underflow. It is frequently assumed that once an inflow has plunged and formed an underflow or interflow, its constituent's load is isolated from the surface waters. Although this situation has been shown to be true in many situations, recent studies (Chen et al., 2006) have indicated that mixing can entrain inflow constituents into surface waters.

It is not uncommon for environmental fluids to be subjected simultaneously to destabilizing effects of a velocity shear (induced by underflow) and to stabilizing effects of density stratification. The outcome of such competition is often the so-called Kelvin-Helmholtz (KH) instability (e.g., DeSilva et al., 1996; Thorpe and Jiang, 1998; Özgökmen and Chassignet, 2002; Umlauf and Lemmin, 2005). The resulting entrainment has been extensively studied elsewhere (e.g., Chung and Gu, 1988; Gu and Chung, 2003).

Improved knowledge of the behavior of density currents is essential to determine the time-space variability of the water characteristics. Density currents may transport undesirable materials such as suspended solids, organic chemicals, or nutrients from the watershed to reservoir downstream (Chen et al., 2006) or may cause sedimentation (Annandale, 1987; De Cesare et al., 2001). Thus, appropriate reservoir operation to avoid sedimentation or water quality deterioration, requires knowledge of density current behavior.

HESSD
8, 1193–1223, 2011

Some studies about density current have been carried out: Feitsui Reservoir (Chen et al., 2006), Lake Ogawara (Dallimore et al., 2001), the Katsyrasawa Reservoir (Chikita, 1989), both in Japan, Lake Geneva in Switzerland (Lambert and Giovanoli, 1988), Lake Onachota and Fayett ville Green Lake in the United States (Ford, 1990), and the Alpine Luzzone Reservoir in Switzerland (De Cesare et al., 2001). In contrast to the above, there have been relatively few or absence of studies about the use of remote sensing to study the density currents in reservoirs.

The available literature tends to focus on the following issues: visible data used to look at changes in the clarity and color of the water (Chipman et al., 2004) associated with changes in sediment input (Mertes et al., 1993) or the amount of chlorophyll (Novo et al., 2006), algal blooms (Duan et al., 2009); thermal infrared data can be used to look at changes in the surface temperature (Alcântara et al., 2010) associated with upwelling (Schladow et al., 2004; Steissberg et al., 2005) or changes in circulation (Ikeda and Emery, 1984).

The authors (Anderson et al., 1995) had deployed a hand-held thermal radiometer to obtain indirect measurements of the water surface temperatures in order to study the influx cold water in reservoirs. However, this kind of data is limited in time and space. The knowledge of the physical, chemical, and biological mechanisms controlling water quality is limited by lack of observations at the necessary spatial density and temporal frequency need to infer the controlling processes. The satellite images ability in get synoptic information with temporal recovering becomes remote sensing a very useful tool to study plunge point location.

The plunge point location provides an indication of where the riverine zone stops and the lakes begins. If the riverine zone extends a significant distance into the reservoir, the reservoir is dominated by advective forces and cannot be considered to be vertically one-dimensional (Arneborg et al., 2004). Since the process occurring in a reservoir is dependent of the river behavior along the reservoir which is strongly determined by the contrast between incoming river and reservoir water, this tool can be applied to study, remotely, some important aspects related to reservoir functioning. It is important

HESSD
8, 1193–1223, 2011

because, depending on location, in situ measurements temperature, such as on the thermistors chains, might not capture the plunge point spatial variability and, consequently, if the inflow will behavior as an under, inter or overflow.

A number of models have been proposed for prediction of plunge depth. These models are generally valid only for channels of constant slope and width. Failure to accurately predict the plunge depth will result in an inaccurate representation of the initial underflow layer thickness and therefore causes a distortion of the underflow dynamics beyond the plunge point (Dallimore et al., 2004).

Based on this, the purpose of this paper is to investigate both the potentiality and applicability of the use of thermal and visible satellite instruments to monitor the density difference between the water body and the inflowing water (plunge point location).

2 Methods

2.1 Field site and measurements

The Manso Reservoir (14°50′ S; 55°45′ W), located in a Savanna biome, has a dendrite shape with 427 km^2 of flooded area, and 60 m of maximum depth (Fig. 1).

The annual mean temperature is 26 °C and total precipitation averages 1750 mm, concentrated during the Austral summer (wet season). Furnas Centrais Elétricas, responsible for operating the reservoir, completed filling the reservoir in 1999. In Manso Reservoir the summer stratification is characterized by temperature differences up to 4 °C between the epilimnion and hypolimnion. Table 1 summarizes the main characteristics of Manso reservoir for the analyzed period.

2.2 Environmental time series

The temporal variability of environmental parameters used here was coverage using the data collected by an anchored buoy system called Environmental Monitoring

HESSD
8, 1193–1223, 2011

System – SIMA. This system is a set of hardware and software projected for data acquisition and real time monitoring of hydrological systems (Stech et al., 2006) with data storage systems, sensors (air temperature, wind direction and intensity, pressure, incoming and reflected radiation and thermistor chain), solar panel, battery and the transmission antenna are fixed.

The data are collected in preprogrammed time interval and are transmitted by satellite in quasi-real time for any user in a range of 2500 km from the acquisition point. The selection of the environmental parameters measured by SIMA (moored near the dam, indicated by Station-13 in Fig. 1) took into account aspects as: relevance as environmental index (i.e., the variables that respond consistently to alterations in the functioning of the aquatic system), importance for the greenhouse gas emission process in aquatic systems, and the technical suitability for data acquisition and transmission from automatic platforms (Stech et al., 2006).

2.3 Environmental profiles

Vertical profiles were measured during wet season (Fig. 1) as follows: (1) eleven stations in the longitudinal direction from the river (1 to 8) towards the dam (10, 12 and 13), following the thalweg; (2) and three stations in the transversal direction. This design allowed for one longitudinal transect composed of 11 profiles and two transversal transects, one near the dam (13 and 14) and the other 20 km far from dam (9, 10 and 11) (Fig. 1).

The stations were spaced 3 km apart in the reservoir and 0.5 km in the river-reservoir transition zone. Vertical profiles of pressure, water temperature (with a resolution of 0.01 °C and 5% accuracy), dissolved oxygen concentration (resolution: 0.01 mg/l and accuracy: 2%), and conductivity (resolution: 1.0 µS/cm and accuracy: 0.5%) were made with a multi-parameter probe (Yellow Springs Instr., model 6600) and a submersible fluorimeter (Satlantic) with a resolution of 0.05 $\mu g\, l^{-1}$ and range of 0–200 $\mu g\, l^{-1}$.

HESSD
8, 1193–1223, 2011

Fifty-six contained Hobo temperature loggers were deployed in five thermistor chains at 1 m intervals from depths 0 to 4 m, and at 3 m intervals from depths 4 to 20 m. The sampling period of the thermistor was 15 min.

2.4 Circulation measurements

Water circulations measurements at the river-reservoir transition zone were carried out using drifters. These drifters were built following the (Sybrandy and Niiler, 1991) design and consist of three parts: a GPS data logger installed in a fiber glass sphere float connected to a drogue in order to reduce the wind slip effect. The drifters were drogued at 6 m, because the focus in the present experiment was the inflow velocity.

The sampling frequency was 0.01 HZ and the positioning precision was 10-m horizontal root mean square. Three drifters were released simultaneously along the river-reservoir transition zone at different positions (stations 1, 3 and 5 in Fig. 1) and collected successive position (latitude and longitude) data continuously for approximately 23 h. The field velocity was estimated from these time series of positions. In order to remove the noise, the resulting time series were filtered using a low-pass filter with a cutoff period of 15 min.

2.5 Computing water surface temperature from Landsat-5-TM data

Generally, the grey level in images of the Thematic Mapper (TM) sensor of Landsat is given as digital number (DN) ranging from 0 to 255 (8 bits). Thus, the computation of brightness temperature from TM6 (thermal band: 10.5–12.5 µm) data includes the estimation of radiance from its DN value and the conversion of the radiance into brightness temperature.

For this purpose, we utilized the equation developed by the National Aeronautics and Space Administration-NASA (Chander et al., 2009). Water vapor content and atmospheric temperature at each layer were approximated using the local meteorological observation data (Qin et al., 2001), measured by the Weather Forecast and

HESSD
8, 1193–1223, 2011

Climatic Studies Center (CPTEC) from the Brazilian National Institute for Space Research (INPE).

2.6 The entrainment velocity, the depth of the plunge point, and Kelvin-Helmholtz instability

Some authors (Britter and Linden, 1980; Monaghan et al., 1999) found from theory and laboratory experiments that the head of density currents travels at a constant speed, U_F, is proportional to a third power of buoyancy flux per unit width, defined as $B_F = g'Q$, where g' (the reduced gravity) is equal to $g\Delta\rho_p/\rho_o$, and $\Delta\rho_p$ is the density difference across the pycnocline, ρ_o is mean density, g is gravity and $Q = h_r U_r$ is the volume flux per unit width, with h_r and U_r being the average thickness and speed of the current at the input location. Studying (Özgökmen and Chassignet, 2002) gravity and density currents, showed that numerical simulations compare well with laboratory measurements and laboratory results are valid on geophysical scales.

For the location of the plunge point, their depth (m) was estimated as in (Ford, 1990):

$$h = 1.6\left(\frac{Q^2}{gL^2\frac{|\Delta\rho|}{\rho}}\right)^{1/3} \quad (1)$$

Where h is the hydraulic plunge point depth (m), $\Delta\rho$ is the difference between the densities of inflow and reservoir (kg/m^3), and L is the width of zone of convergence (m).

The density function, developed by (Gill, 1982; Ford, 1990), is

$$\rho = \rho_{Tw} + \Delta\rho_s \quad (2)$$

$$\rho_{Tw} = 999.8452594 + 6.793952\times10^{-2}T_w - 9.095290\times10^{-3}T_w^2 + 1.001685\times10^{-4}T_w^3 - 1.120083\times10^{-6}T_w^4 + 6.536332\times10^{-9}T_w^5 \quad (3)$$

HESSD
8, 1193–1223, 2011

$$\Delta\rho_s = C_{ss}\left(1-\frac{1}{sg}\right)\times 10^{-3} = 0.00062C_{ss} \quad (4)$$

Where ρ_{T_w} is the density of water that is a function of water temperature (T_w), $\Delta\rho_s$ is the density increment owing to the concentration of suspended solids (C_{ss}), and sg is the specific gravity of suspended solids (assumed as in Chen et al., 2006).

The entrainment coefficient, E, the normal depth of the underflow along the centerline, h_c, were calculated as Chen et al. (2006):

$$E = \frac{1}{2}C_k C_d^{3/2} F^2 \quad (5)$$

$$h_c = \frac{6E}{5}\times + h_r \quad (6)$$

Where x is the distance downstream from the plunge point, and F is the Froude Number at a plunge point:

$$F^2 = \frac{U_r^2}{g\frac{|\Delta\rho|}{\rho}h} \quad (7)$$

The slope, together with the density difference, provides the forcing of the flow against friction. The mean slope of the reservoir bed (s) is about 30/40 000, approximately 0.00075, and the drag coefficient (c_d) was assumed equal to about 0.003 as in (Arneborg et al., 2004). A model of a frictionally balanced gravity current (Stigebrandt, 1987) was used in order to compare the speed (u) estimated by the model $U_r = \left(\frac{s}{c_d} g\frac{\Delta\rho}{\rho}h\right)^{1/2}$ with that measured by drifter. The friction velocity was calculated as $u_* = \sqrt{(\rho_a/\rho_w)C_d V^2}$, where V in ($m\,s^{-1}$) is the surface wind speed, $\rho_a = 1.2\,kg\,m^{-3}$ is the air density and C_D is a drag coefficient.

HESSD
8, 1193–1223, 2011

3 Results and discussions

3.1 Thermal structure

Temporal patterns of rainfall, wind and air temperature (Fig. 2a) and short and long wave radiation (Fig. 2b), show that daily precipitation can exceed 80 mm in the wet season period. As it will be detailed below, the resulting increases in the inflow have a strong effect on the thermal structure of the reservoir during the wet season. In the dry season, it is easily seen the long-term decrease trend in short wave radiation and increase in wind speed.

From end of April and July, seven cold fronts events reached Manso Reservoir (arrows in Fig. 2a). Further details about the action of cold front in Manso Reservoir can be found in Lorenzzetti et al. (2005). Note that each peak of the wind speed is associated with a steep fall of air temperature during the cold front passage. Air temperatures declined of about 6 °C during these events and daily average wind reached 6 m s^{-1}.

As latent and sensible flux terms are almost linearly dependent on wind and the short wave drops during the cold front passage, the net surface radiation becomes negative and reservoir loses (latent) heat to the atmosphere (not shown). Thus, the deepening of the surface mixing layer due to the stirring from the wind stress will be enhanced by downward convective mixing in dry seasons.

The thermal stratification in Manso Reservoir is moderate and is spread over a thick metalimnion in the first half of the analyzed period (2 February–30 April) (Figs. 3 and 4). The metalimnion extends from 7–25 m, with temperatures ranging from 28–30 °C. During this period, wind speed was on average 2.3 ± 0.5 m s^{-1} without any predominant direction. Due to the weaker winds, the atmosphere's reservoir boundary layer is less turbulent, advection and diffusive contributions to sensible heat flux and evaporation are all small, and the radiational heat input is concentrated in a shallower surface layer (Fig. 3).

During wet season-stratified period, the thick metalimnion and moderate stratification could make Manso Reservoir susceptible to partial upwelling, i.e., metalimnetic water

HESSD
8, 1193–1223, 2011

reaching the surface. However, analysis based on Wedderburn and Lake Number (not shown) indicated that the wind-driven upwelling/downwelling was unimportant during wet season. Some enhanced mixing events are visible during 16–19 February, 18–21 March, and 6–9 May, when 28 °C water was transported to the surface.

In the next section, we show evidences about the river contribution to enhancing mixing process indicated by arrows in Fig. 3. The reservoir thermal structure (Fig. 4) suggests that in the wet season, the river stays at hypolimnion level and contributes to the thermal stability of the water column. This situation persists during the wet season. In the dry season, the river circulation is characterized by interflow-overflow as discussed below.

3.2 River effects in thermal structure and Kelvin-Helmholtz instability

In situ measurements during the wet season showed a high contrast between the suspended solid concentration in the reservoir ($4.2\,mg\,l^{-1}$) and river ($15.0\,mg\,l^{-1}$). This contrast can be easily observed in satellite images (Fig. 5a). This contrast is also observed in the surface water temperatures (Fig. 5b).

Note that in Fig. 5 there is a difference of approximately 5.40 km in the plunging point location measured by satellite image acquired in the visible spectrum (Fig. 5a) and that in the thermal region (Fig. 5b) during the wet season. This difference can be explained by the fact that the solar radiation interacts with upper most water column optically active components (such as: chlorophyll, inorganic particles and dissolved organic matter) whereas the thermal radiation detects skin temperatures.

The turbidity currents can be observed in Fig. 5a travelling underwater until they reach a depth at which the sensor can not longer detect them. Thus, the true plunge point position is given by the thermal image. In the dry season the plunging point location in the visible satellite image (Fig. 5c) is coincident with that of the thermal image (Fig. 5d).

As pointed out by Ford (1990), these water density differences that are mainly caused by differences in temperature, dissolved and suspended solids in the river-reservoir

HESSD
8, 1193–1223, 2011

transition. According to Akiyama and Stefan (1984) these physicochemical patterns cause density differences between reservoir and river waters which are responsible by plunging inflows.

Manso Reservoir experiences large seasonal as well as short time runoff variations, resulting in inflow variations presenting an intermittent pattern with large inflows during the summer-autumn months (Fig. 6). If moving with a propagation speed $u \sim 0.1\,\mathrm{ms}^{-1}$ (as estimated by model and confirmed by drifters) and a distance of 23 km, one obtains the propagation time ~ 2.5 days (because the signal of inflow must be propagate 23 km downstream – from upstream until thermistor chain). This result suggests that the underflow is an important mechanism driving thermocline displacement.

The river progressively sinks down to the level of the thermocline and contributes to the thermal stability of the water column in wet season (Fig. 7). After the inflow plunges, it can follow the thalweg as an underflow partially enhanced by downstream turbine and spillway outflows (outflow at Manso ~ 15 m).

The river showed similar temperature, conductivity, and pH to that of the hypolimnion (Figs. 7, 8) at dam area (39 km downstream of the river) indicating that the river followed the thalweg as an underflow. In this case, it is expected during the wet season the following fluid behavior: a denser fluid enters a domain and flows under lighter fluid, waves develop along the interface (due shear velocity), these waves grow in the downstream direction, develop into billows and eventually roll up. This behavior is indicative of the Kelvin-Helmholtz instability in which waves made up of fluid from the current (river) entrap the ambient fluids (Thorpe and Jiang, 1998; Corcos and Sherman, 2005).

This fact suggests that the inflow exerts controls on residence time for Manso Reservoir, as verified by (Rueda et al., 2006) at the Sau Reservoir. The usual condition for the onset of Kelvin-Helmholtz instability is that the gradient Richardson Number $Ri = \frac{g}{\rho_o}\frac{\partial \rho}{\partial z}\left|\frac{\partial U}{\partial z}\right|^{-2}$ must be lower than a critical value, tipically $Ri_{\mathrm{crit}} \cong 0.25$.

Experimental researches suggest that vertical mixing in stratified fluids away from the direct effects of boundaries is Richardson Number dependent. Some authors (Kunze et

HESSD
8, 1193–1223, 2011

al., 1990; Trowbridge, 1992; Peters and Gregg, 1995; Baringer and Price, 1997) shows that the *Ri* estimates are very sensitive to the length scale over which the vertical gradients are calculated. Thus, we apply in our analysis an alternative to *Ri* estimates for a two-layer flow. Such bulk analysis was performed by (Cushman-Roisin, 2005) and yields a criterion for the vertical extent of the eventual mixing. If the following inequality holds true $\frac{(\rho_2-\rho_1)gH}{\rho_o(U_1-U_2)^2} < 1$, then vertical mixing is energetically possible. Estimates of U_1 obtained from u^* and U_2 calculated from the inflow and measured by drifters (shown in next subsection) indicate that this inequality was verified during the wet season, indicating that the Kelvin-Helmholtz may play a strong role in the thermocline displacement during the wet season.

During dry season, the decrease in river flow and the decrease in density differences (Fig. 5d) lead to river circulation characterized by inter-overflow. As discussed, in this period occur many cold front passages. Thus, important energetic mixing process are driven by wind and by surface cooling during dry season due cold front action, and hence the close the river water is to the surface, the higher is the probability that it experiences mixing with reservoir waters.

An inter-overflow situation may have important influence on reservoir water quality by introducing oxygen-demanding material, nutrients, and bacteria directly into the surface waters or euphotic zone (Alavian et al., 1992). Available nutrients can be assimilated by phytoplankton and may stimulate plankton blooms. In the downstream direction where an inter-overflow hit the dam construction could occur the accumulation of phytoplankton as seen from satellite imagery (Fig. 9). This process affects the water quality: concentrations of suspended solids at surface varied from 2.2 to 4.8 $\mathrm{mg\,l^{-1}}$ (dry season – inter-overflow) and dropped to the range between 0 to 1.0 $\mathrm{mg\,l^{-1}}$ (rainy season – underflow) in the reservoir, while in the river this concentration was 15 $\mathrm{mg\,l^{-1}}$ and 10 $\mathrm{mg\,l^{-1}}$, respectively.

Therefore, the larger values observed in July (although a dry month) would be due to river waters insertion into the reservoir upper layers, as an inter-overflow. This process was also depicted in the water transparency (Secchi disk) in Manso Reservoir when

HESSD
8, 1193–1223, 2011

the transparency dropped from 5.5 m to 4.5 m. Through these results we will pass to discuss the plunging underflow in more detail.

3.3 Analysis of a plunging underflow

The important density current parameters (i.e., propagation speed, thickness, and the point of plunging) can be used to determine a change in water quality at different depths (Alavian et al., 1992). Despite of the limited predictive ability of empirical models, due the complex bathymetry of real reservoirs and continuous rather than layered stratification (Dallimore et al., 2004), what indicates the need for observations of density currents; we used the simplified one-dimensional model (Eqs. 1–7) to estimate and compare with hydrological data. The hydrological conditions show in Fig. 10 and the average inflow water temperature 26.5 °C were utilized.

Based on the measured suspended solid concentrations at the river, the inflow suspended solids concentrations was 15 mg l^{-1}. The estimated total density of the inflow including the density increment due to suspended solids was 996.53 kg m^{-3}. The receiving mean water temperature was 28 °C, and the density difference between the inflow and receiving water was 0.62 kg m^{-3}. The Froude Number (Eq. 7) of the flow was estimated to be 0.198 and the estimated depth of the plunge point was 10.5 m, which is close to the observed depth, 12 m (Fig. 10). The entrainment coefficient, E, was 0.00031.

Applying h in Eq. (6), the greatest depth (h_c) that would have been reached by the density current was estimated to be 14.5 m at $x = 20$ km. This estimated value is very close to that observed from the thermistor chain positioned at 20 km downstream (Fig. 11). The simulation result is thus consistent with the observed data.

HESSD
8, 1193–1223, 2011

4 Conclusions

With the objective of monitoring the plunging point location in the Manso hydroelectric reservoir the following conclusions was possible:

- The spatial variability of the plunge point evident in the hydrologic data illustrates the advantages of synoptic satellite measurements over in situ point measurements alone to detect the river-reservoir transition zone.
- For wet season the upward entrainment engendered by the Kelvin-Helmholtz instability was the main mixing mechanism in reservoir waters.
- During dry season, when occur the nearly homogeneity between river and reservoir water temperature, strong turbulence introduced by high winds and surface cooling were predominant.
- The jointly use of thermal and visible channel, operational monitoring of plunge point is feasible. The deduced information about the density current from this product could potentially be assimilated for numerical modeling and hence be of significant interest for environmental and climatological research.

Acknowledgements. This work was supported by the "Carbon Budgets of Hydroeletric Reservoirs of Furnas Centrais Elétricas S. A." The authors are grateful to the Brazilian Council for Scientific and Technological Development (CNPq) under grants 482488/2007-7.

References

Alcântara, E. H., Stech, J. L., Lorenzzetti, J. A., Bonnet, M-P., Casamitjana, X., Assireu, A. T., and Novo, E. M. L. M.: Remote sensing of water surface temperature and heat flux over a tropical hydroelectric reservoir, Remote Sens. Environ., 114, 2651–2665, 2010.

Alavian, V., Jirka, G. H., Denton, R. A., Johnson, M. C., and Stefan, H. G.: Density currents entering lakes and reservoirs, J. Hydraul. Eng.-ASCE, 18, 1464–1489, 1992.

HESSD

8, 1193–1223, 2011

Anderson, J. M., Duck, R. W., and Mcmanus, J.: Thermal radiometry: a rapid means of determining surface water temperature variations in lakes and reservoirs, J. Hydrol., 173, 131–144, 1995.
Annandale, G. W.: Reservoir sedimentation, Elsevier Science Publishers, Amsterdam, 1987.
Akiyama, J. and Stefan, H. G.: Plunging flow into reservoir, Theor. J. Hydraul. Eng.-ASCE, 110, 484–499, 1984.
Arneborg, L., Erlandsson, B. L., and Stigebrandt, A.: The rate of inflow and mixing during deep-water renewal in a sill fjord, Limnol. Oceanogr., 49, 768–777, 2004.
Baringer, M. O. and Price, J. F.: Momentum and energy balance of the Mediterranean outflow, J. Phys. Oceanogr., 27, 1678–1692, 1997.
Baxter, R. M.: Environmental effects of dams and Impoundments, Ann. Rev. Ecol. Syst., 8, 255–283, 1997.
Britter, R. E. and Linden, P. F.: The motion of the front of a gravity current traveling down an incline, J. Fluid Mech., 99, 531–543, 1980.
Chander, Q., Markham, B. L., and Helder, D. L.: Summary of current radiometric calibration coefficients for Landsat MSS, TM, ETM+, and EO-1 ALI sensors, Remote Sens. Environ., 113, 893–903, 2009.
Chen, Y. J., Wu, S. C., Lee, B. S., and Hung, C. C.: Behavior of storm-induced suspension interflow in subtropical Feitsui Reservoir, Taiwan, Limnol. Oceanogr., 51, 1125–1133, 2006.
Chikita, K.: A field study on turbidity currents initiated from spring runoffs, Water Resour. Res., 25, 257–271, 1989.
Chipman, J. W., Lillesand, T. M., Schmaltz, J. E., Leale, J. E., and Nordheim, M. J.: Mapping lake water clarity with Landsat images in Wisconsin, USA, Can. J. Remote Sens., 30, 1–7, 2004.
Chung, S. and Gu, R.: Two-dimensional simulation of contaminant currents in a stratified reservoir, J. Hydraul. Eng.-ASCE, 124, 704–711, 1988.
Corcos, G. M. and Sherman, F. S.: The mixing layer: deterministic models of a turbulent flow, J. Fluid Mech., 139, 29–65, 2005.
Cushman-Roisin, B.: Kelvin-Helmholtz instability as a boundary-value problem, J. Fluid Mech., 5, 507–525, 2005.
Dallimore, C. J., Imberger, J., and Ishikawa, T.: Entrainment and turbulence in saline underflow in Lake Ogawara, J. Hydraul. Eng.-ASCE, 127, 937–947, 2001.
Dallimore, C. J., Imberger, J., and Hodges, B. R.: Modeling a plunging underflow, J. Hydraul.

HESSD
8, 1193–1223, 2011

Eng.-ASCE, 130, 1068–1076, 2004.
De Cesare, C., Schleiss, A., and Hermann, F.: Impact of turbidity currents on reservoir sedimentation, J. Hydraul. Eng.-ASCE, 127, 6–16, 2001.
DeSilva, I., Fernando, H. J. S., Eaton, F., and Hebert, D.: Evolution of Kelvin-Helmholtz billows in nature and laboratory, Earth Planet. Sci. Lett., 143, 217–231, 1996.
Duan, H., Ma, R., Xu, X., Kong, F., Zhang, S., Kong, W., Hao, J., and Shang, L.: Two-decade reconstruction of algal blooms in china's lake taihu, Environ. Sci. Technol., 43, 3522–3528, 2009.
Ford, D. E.: Reservoir transport processes, in: Reservoir Limnology: Ecological Perspectives, edited by: Thornton, K. W., Kimmel, B. L., and Payne, F. E., Wiley-Interscience, New York, 15–41, 1990.
Gill, A. E.: Appendix 3: properties of seawater, in: Atmosphere-ocean dynamics, edited by: Gill, A. E., Academic Press, New York, 1982.
Gu, R. and Chung, S.: A two-dimensional model for simulating the transport and fate of toxic chemicals in a stratified reservoir, J. Environ. Qual., 32, 620–632, 2003.
Ikeda, M. and Emery, W. J.: A continental-shelf upwelling event off Vancouver Island as revealed by satellite infrared imagery, J. Mar. Res., 42, 303–317, 1984.
Kunze, E., Williams, A. J., and Briscoe, M. G.: Observations of shear and vertical stability from a neutrally buoyant float, J. Geophys. Res., 95, 18127–18142, 1990.
Lambert, A. and Giovanoli, F.: Records of riverborne turbidity currents and indications of slope failures in the Rhone Delta of Lake Geneva, Limnol. Oceanogr., 33, 458–468, 1988.
Lorenzzetti, J. A., Stech, J. L., Assireu, A. T., Novo, E. M. L. M., and Lima, I. B. T.: SIMA: a near real time buoy acquisition and telemetry system as a support for limnological studies, in: Global warming and hydroelectric reservoirs, edited by: Santos, M. A. and Rosa, L. P., COPPE: Rio de Janeiro, 71–79, 2005.
Martin, J. L. and McCutcheon, S. C.: Hydrodynamics and transport for water quality modeling, Lewis, Boca Raton, Florida, USA, 1999.
Mertes, L. A. K., Smith, M. O., and Adams, J. B.: Estimating suspended sediment concentrations in surface waters of the Amazon River wetlands from Landsat images, Remote Sens. Environ., 43, 281–301, 1993.
Monaghan, J. J., Cas, R. A. F., Kos, A. M., and Halworth, M.: Gravity currents descending a ramp in a stratified tank, J. Fluid Mech., 379, 39–70, 1999.
Novo, E. M. L. M., Barbosa, C. C., Freitas, R. M., Shimabukuro, Y. E., Melack, J. M., and Pereira

HESSD
8, 1193–1223, 2011

Filho, W.: Seasonal changes in chlorophyll distributions in Amazon floodplain lakes derived from MODIS images, Limnology, 7, 153–161, 2006.
Özgökmen, T. M. and Chassignet, E. P.: Dynamics of two-dimensional turbulent bottom gravity currents, J. Phys. Oceanogr., 32, 1460–1478, 2002.
Peters, H., Gregg, M. C., and Sanford, T. B.: Detail and scaling of turbulent overturns in the Pacific equatorial undercurrent, J. Geophys. Res., 100, 18349–18368, 1995.
Poff, N. L. and Hart, D. D.: How dams vary and why it matters for the emerging science of dam removal, Bioscience, 52, 659–668, 2002.
Qin, Z., Karnieli, A., and Berliner, P.: A mono-window algorithm for retrieving land surface temperature from Landsat TM data and its application to the Israel-Egypt border region, Int. J. Remote Sens., 22, 3719–3746, 2001.
Ramos, F. M., Lima, I. B. T., Rosa, R. R., Mazzi, E. A., Carvalho, J. C., Rasera, M. F. F. L., Ometto, J. P. H. B., Assireu, A. T., and Stech, J. L.: Extreme event dynamics in methane ebullition fluxes from tropical reservoirs, Geophys. Res. Lett., 33, L21404, doi:10.1029/2006GL027943, 2006.
Rueda, F., Moreno-Ostos, E., and Armengol, J.: The residence time of river water in reservoirs, Ecol. Modell., 191, 260–274, 2006.
Schladow, S. G., Palmarsson, S. O., Steissberg, T. E., Hook, S. J., and Prata, F. J.: An extraordinary upwelling event in a deep thermally stratified lake, Geophys. Res. Lett., 31, 1–4, 2004.
Stech, J. L., Lima, I. B. T., Novo, E. M. L. M., Silva, C. M., Assireu, A. T., Lorenzzetti, J. A., Carvalho, J. C., Barbosa, C. C., and Rosa, R. R.: Telemetric monitoring system for meteorological and limnological data acquisition, Verh. Internat. Verein. Limnol., 29, 1747–1750, 2006.
Stigebrandt, A.: A model for the vertical circulation of the Baltic deep water, J. Phys. Oceanogr., 17, 1772–1785, 1987.
Steissberg, T. E., Hook, S. J., and Schladow, S. G.: Characterizing partial upwelling and surface circulation at Lake Tahoe, California-Nevada, USA, with thermal infrared images, Remote Sens. Environ., 99, 2–15, 2005.
Sybrandy, A. L. and Niiler, P. P.: WOCE/TOGA Lagrangian drifter-construction manual, University of California, California, 1991.
Thorpe, S. A. and Jiang, R.: Estimating internal waves and diapycnal mixing from conventional mooring data in a lake, Limnol. Oceanogr., 43, 936–945, 1998.

HESSD
8, 1193–1223, 2011

Trowbridge, J. H.: A simple description of the deepening and structure of a stably stratified flow driven by a surface stress, J. Geophys. Res., 97, 15529–15543, 1992.
Umlauf, L. and Lemmin, U.: Interbasin exchange and mixing in the hypolimnion of a large lake: the role of long internal waves, Limnol. Oceanogr., 50, 1601–1611, 2005.

HESSD
8, 1193–1223, 2011

Table 1. General characteristics of the Manso Reservoir.

	Wet season (Feb–Apr)	Dry season (May–Jul)
Average air temperature	27.0 °C	24.0 °C
Total precipitation	615.0 mm	22.0 mm
Extreme air temperatures	24.1–29.9 °C	15.2 – 28.2 °C
Inflow	294.0 $m^3 s^{-1}$	107.0 $m^3 s^{-1}$
Outflow	214.0 $m^3 s^{-1}$	173 $m^3 s^{-1}$
Surface area	372 km^2	365 km^2
Reservoir volume	2610 hm^3	2259 hm^3
Average depth	20 m	18 m
Maximum depth	60 m	58 m
Depth of turbine intakes	34 m	32 m
Latitude, longitude	14°50′ S, 55°45′ W	
Dammed rivers	Manso and Casca	
Year of reservoir filling	1999	

HESSD
8, 1193–1223, 2011

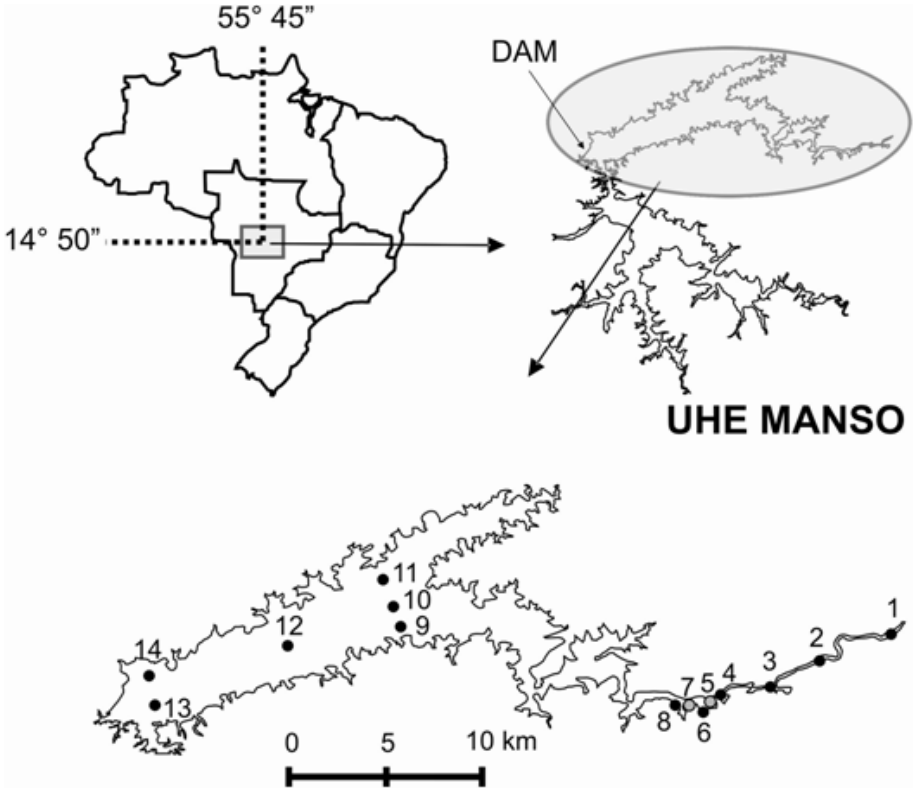

Fig. 1. Study area; grey circles (temperature, fluorescence and photosynthetically available radiation PAR) and filled circles (temperature, conductivity, dissolved oxygen, fluorescence and photosynthetically available radiation PAR) mark the sampling and transect stations. The position 13 indicates also the location of limnolo-meteorological station (SIMA), called here MAN-13. The location of the thermistor chain and drifters deployment are indicated by position 8.

HESSD
8, 1193–1223, 2011

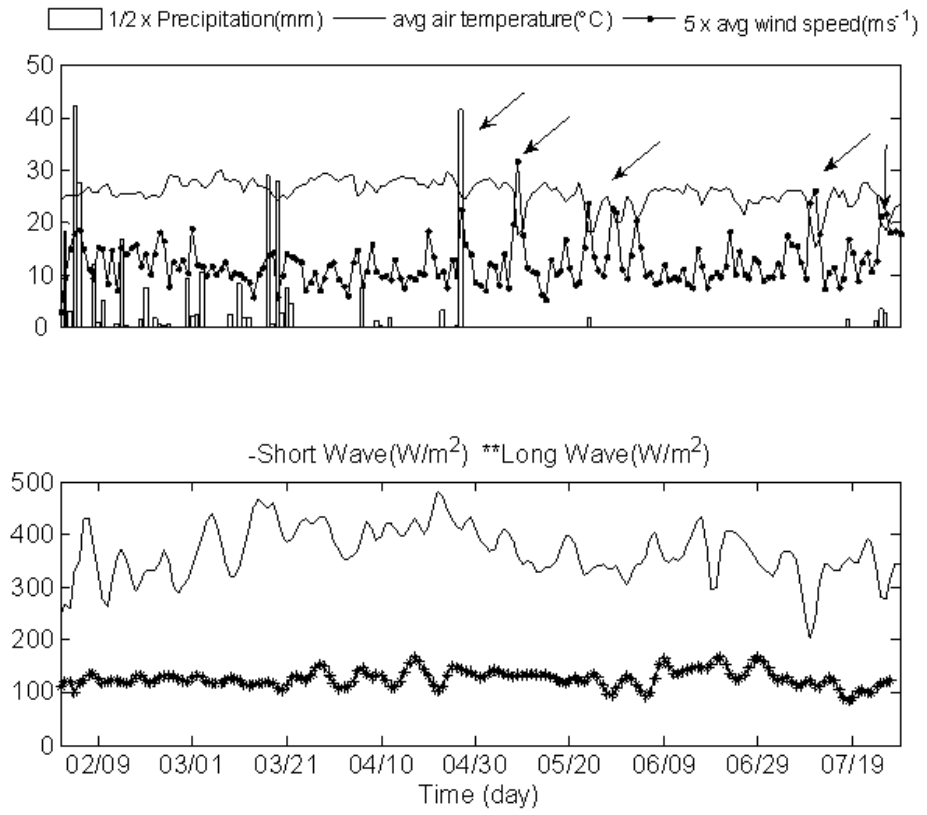

Fig. 2. Daily means of air temperature, wind speed and precipitation (upper panel) and daily mean of solar short wave radiation and long wave fluxes from February to July 2007.

HESSD
8, 1193–1223, 2011

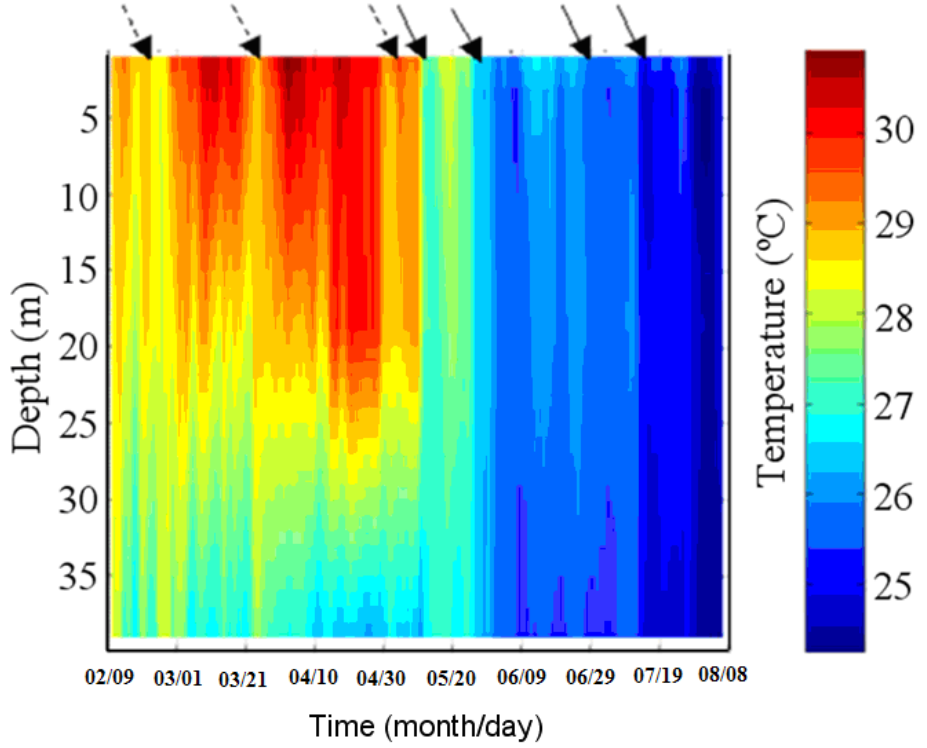

Fig. 3. Temperature contours (°C) from thermistor-chain data measured near the dam.

HESSD
8, 1193–1223, 2011

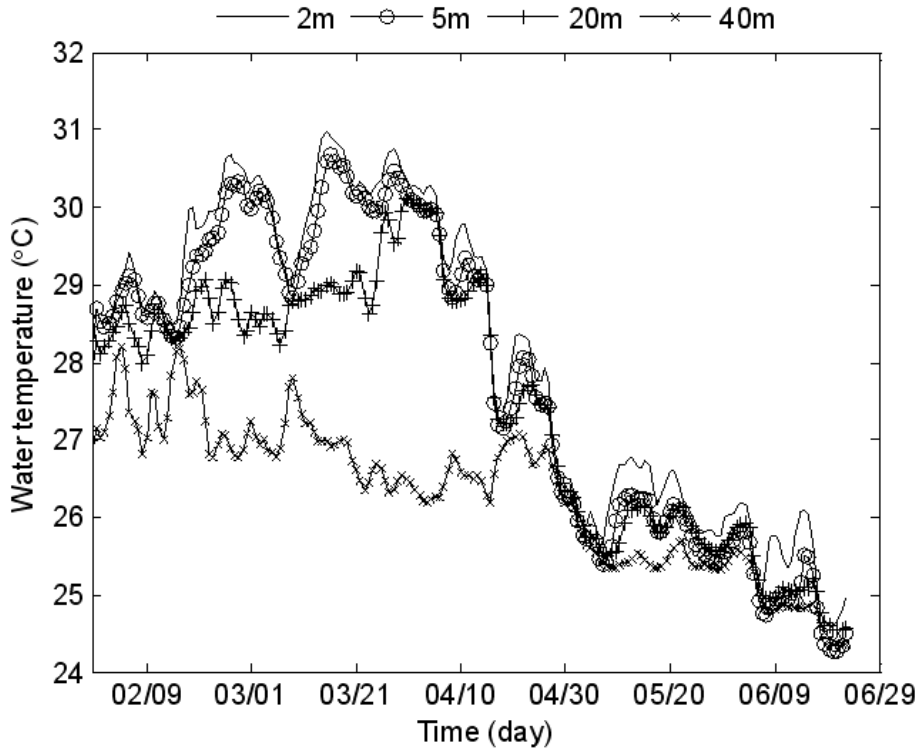

Fig. 4. Thermal structure through the time at Station 13.

HESSD
8, 1193–1223, 2011

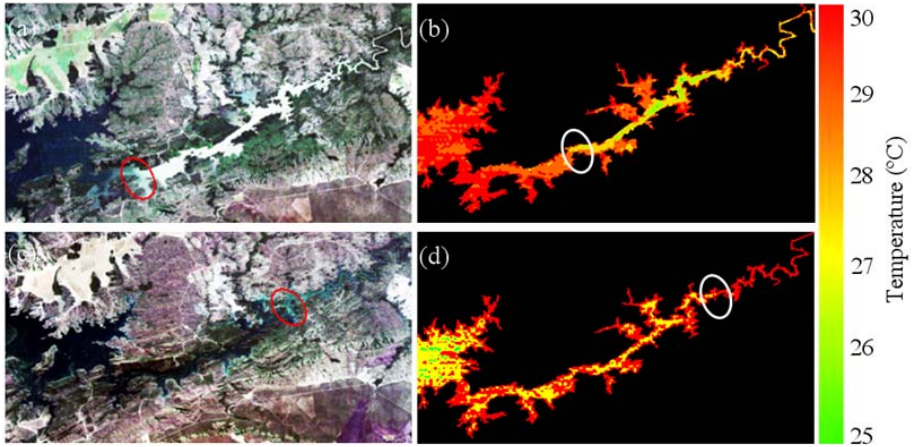

Fig. 5. Satellite images (in true colour composition) acquired on 26 March **(a)** and 16 July **(c)**, showing seasonal plunge point variation (red circle) and the water surface temperature **(b, d)** estimated from thermal band (band 6) of Landsat-5-TM.

HESSD
8, 1193–1223, 2011

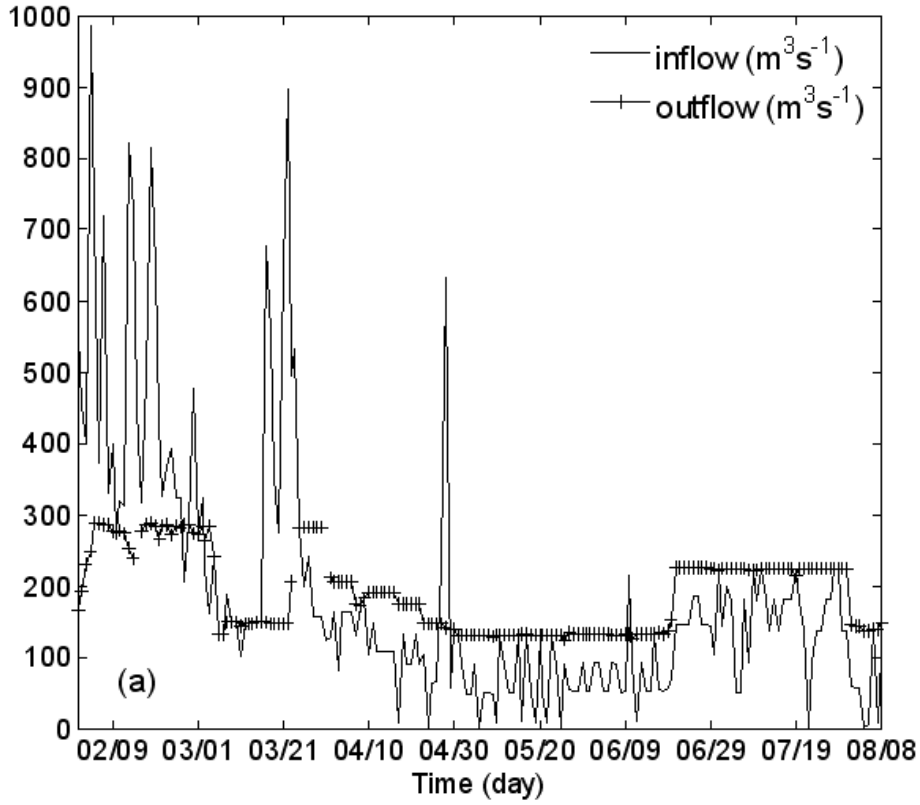

Fig. 6. Inflow and outflow through time.

HESSD
8, 1193–1223, 2011

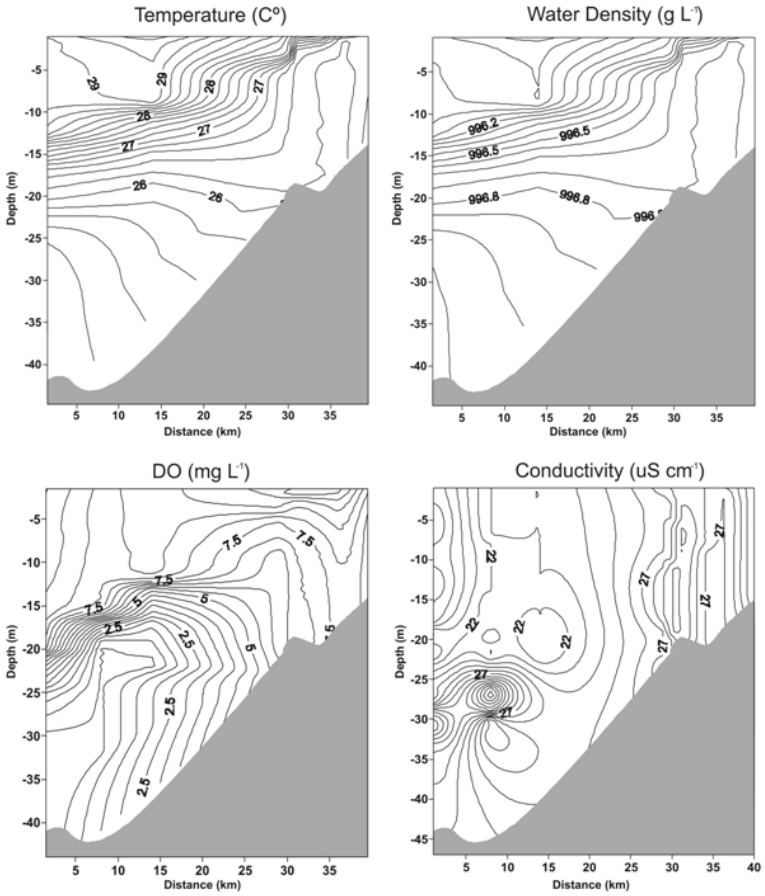

Fig. 7. Isopleths of the **(a)** water temperature, **(b)** density, **(c)** dissolved oxygen and **(d)** conductivity in Manso Reservoir for March (wet season).

HESSD
8, 1193–1223, 2011

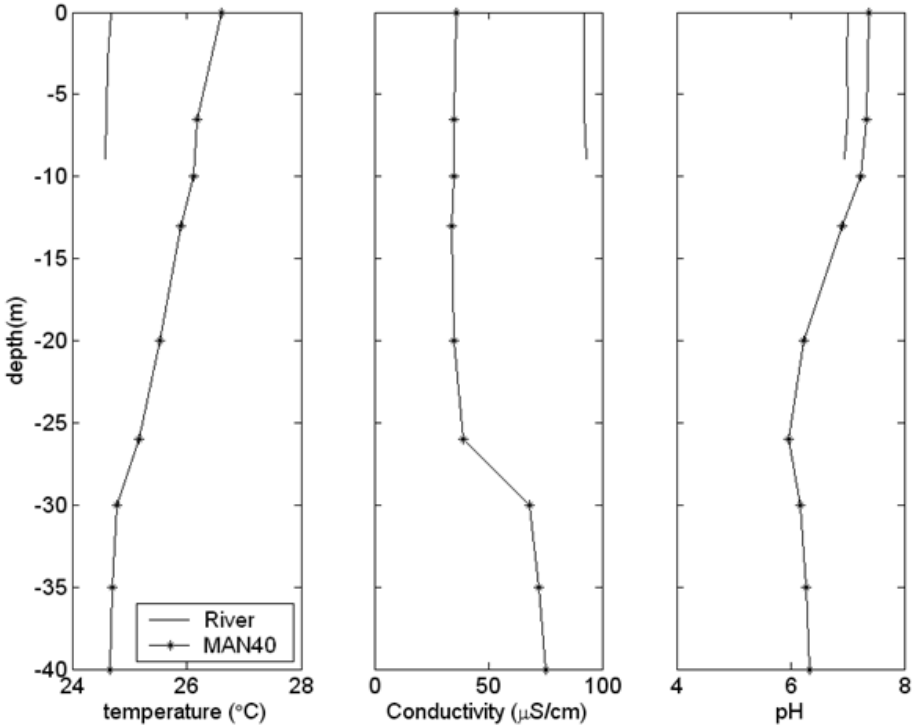

Fig. 8. Temperature, conductivity, and pH vertical profiles at Manso Reservoir measured in river and MAN40 station during wet season.

HESSD
8, 1193–1223, 2011

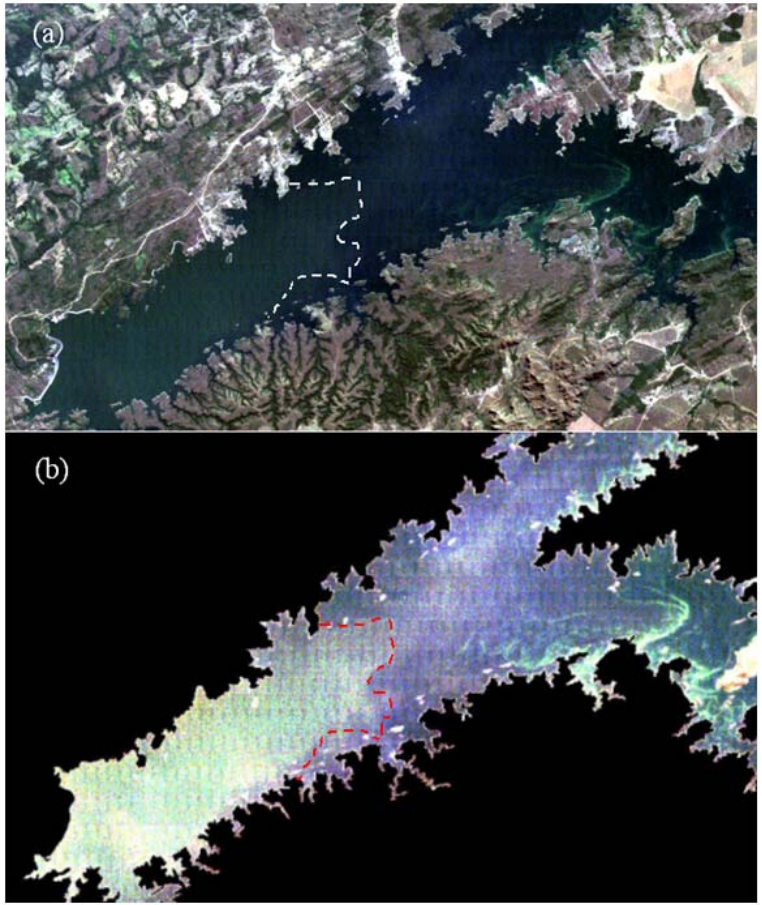

Fig. 9. (a) Satellite imagery in a normal composition (RGB-321) showing the area under Chlorophyll bloom (left to dashed contour). **(b)** The same satellite imagery with land mask and enhanced contrast to better discriminate the phytoplankton bloom.

HESSD
8, 1193–1223, 2011

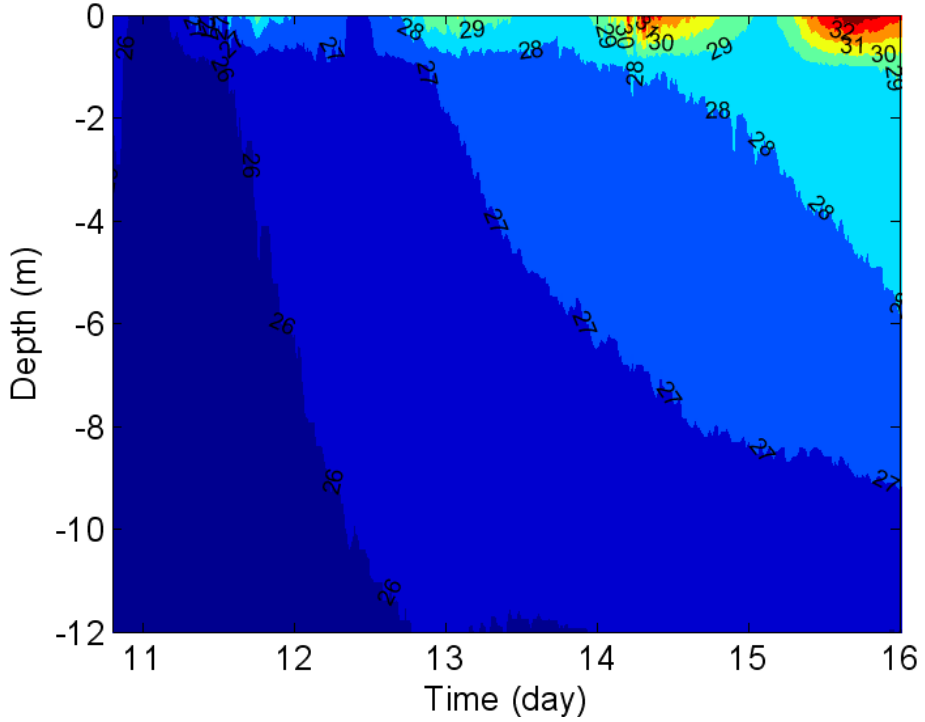

Fig. 10. Temperature contours from thermistor-chain data measured at the river-reservoir transition zone.

HESSD
8, 1193–1223, 2011

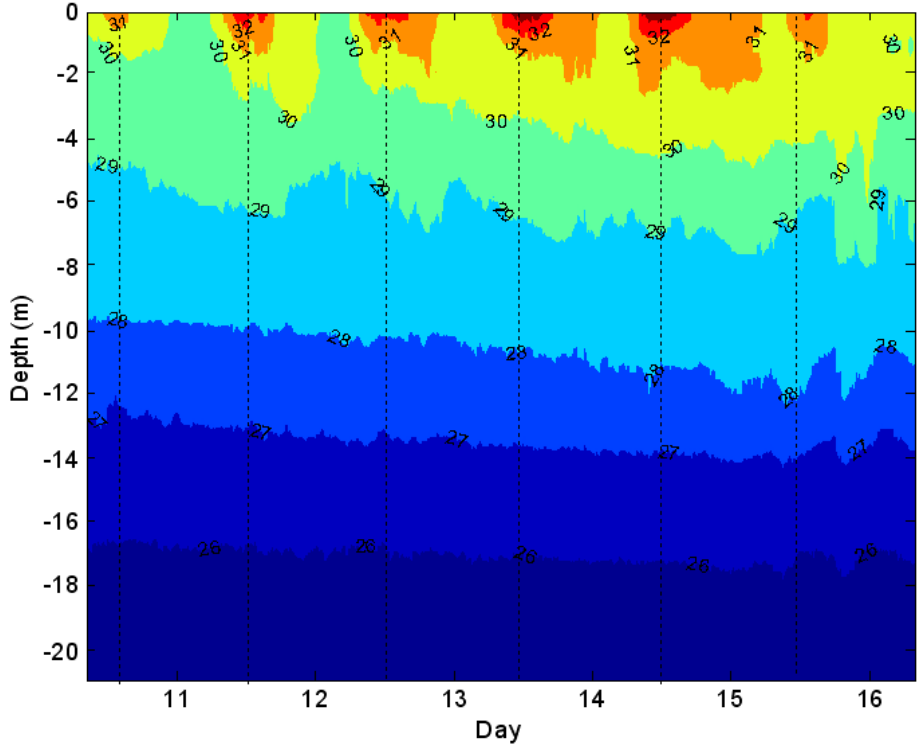

Fig. 11. Temperature contours from thermistor-chain data measured near the dam.

HESSD
8, 1193–1223, 2011